IJMMM International Journal of Minerals, Metallurgy and Materials 矿物冶金与材料学报（英文版）

Establishing optical indicators for the state of hydrogen in MgH_2

Yuxuan Liu, Tingyan Wang, Man Shu, Jianghao Cai, Xiaotian Tang, Tongao Yao, Zhuoran Xu, Zhengyang Gao, Juan Chen, and Weijie Yang

Cite this article as:
Yuxuan Liu, Tingyan Wang, Man Shu, Jianghao Cai, Xiaotian Tang, Tongao Yao, Zhuoran Xu, Zhengyang Gao, Juan Chen, and Weijie Yang, Establishing optical indicators for the state of hydrogen in MgH_2, *Int. J. Miner. Metall. Mater.*, 33(2026), No. 5, pp. 1436-1447. https://doi.org/10.1007/s12613-025-3284-6

View the article online at SpringerLink or IJMMM Webpage.

INTERNATIONAL JOURNAL OF
Minerals, Metallurgy and Materials

Volume 33, Number 5, May 2026
Page 1436

Research Article https://doi.org/10.1007/s12613-025-3284-6

Establishing optical indicators for the state of hydrogen in MgH_2

Yuxuan Liu[1,2),*], *Tingyan Wang*[3),*], *Man Shu*[1,2)], *Jianghao Cai*[1,2)], *Xiaotian Tang*[1,2)], *Tongao Yao*[1,2)], *Zhuoran Xu*[1,2)], *Zhengyang Gao*[1,2)], *Juan Chen*[3),✉], *and Weijie Yang*[1,2),✉]

1) Department of Power Engineering, North China Electric Power University, Baoding 071003, China
2) Hebei Key Laboratory of Energy Storage and Integrated Energy Systems, North China Electric Power University, Baoding 071003, China
3) National Engineering Research Center of Light Alloy Net Forming and State Key Laboratory of Metal Matrix Composite, School of Materials Science and Engineering, Shanghai Jiao Tong University, Shanghai 200240, China
(Received: 18 July 2025; revised: 18 September 2025; accepted: 19 September 2025)

Abstract: Accurate determination of the state of hydrogen (SOH) in solid-state hydrogen storage materials is essential not only for optimizing hydrogen release kinetics and enhancing storage efficiency but also for ensuring system safety in practical applications. While most existing studies have concentrated on thermodynamics and kinetics, direct monitoring of residual hydrogen content, a parameter of critical engineering relevance, has rarely been reported. This highlights the urgent need to realize online SOH detection through new physical properties. In this study, we propose a non-invasive, real-time SOH monitoring strategy for magnesium hydride (MgH_2), based on optical properties and combining density functional theory (DFT)-based optical calculations with experimental validation. Using DFT, the optical properties of MgH_2 and its dehydrogenated form (Mg) were systematically calculated across the infrared, visible, and ultraviolet spectral ranges. Theoretical results revealed strong linear correlations between SOH and specific optical parameters, such as reflectance at 1200 nm and 550 nm and refractive index at 250 nm, with the coefficient of determination exceeding 0.99 and mean absolute errors below 0.05. To validate these predictions, reflectance measurements were conducted at 940 nm, a wavelength identified as highly sensitive to hydrogenation, and a consistent decrease in reflectance with increasing hydrogen uptake was observed. The underlying mechanism was attributed to band structure evolution and electron density redistribution, supported by density of states analysis and Drude model interpretations. This work establishes a robust theoretical and experimental framework for optical SOH diagnostics, emphasizes the importance of residual hydrogen detection for advancing solid-state hydrogen storage from fundamental research toward practical engineering applications, and provides new insights into the design of intelligent, optically responsive hydrogen storage systems, paving the way for the development of spectroscopic SOH sensors in next-generation hydrogen energy technologies.

Keywords: magnesium hydride; state of hydrogen; density functional theory; optical properties; reflectance measurements

1. Introduction

Hydrogen energy, with its zero emissions and high energy density, is widely recognized as a promising solution to rising global energy demand and escalating environmental challenges [1–6]. As a clean and low-carbon energy carrier, hydrogen provides a viable alternative to fossil fuels, mitigating air pollution and enhancing ecological sustainability [7–10]. Furthermore, its storage capacity allows hydrogen to mitigate the intermittency of renewable sources such as solar and wind, thereby improving the reliability and resilience of modern power systems [11]. Among the various hydrogen storage technologies, solid-state storage based on metal hydrides stands out due to its high volumetric hydrogen density, intrinsic safety, and operational stability under ambient conditions [12–17].

Solid-state hydrogen storage technology demonstrates considerable potential for efficient hydrogen retention [18–23]. Nevertheless, several technical challenges remain unresolved [24–30]. Among them, one of the most critical investigated issues is the accurate assessment of the state of hydrogen (SOH) within storage materials. Precise SOH monitoring is essential, as it directly influences hydrogen release kinetics, storage capacity, system safety, and operational durability. Conventional SOH detection techniques, including pressure–composition–temperature (PCT) measurements [31] and mass flow monitoring, remain the most commonly employed methods. However, both approaches suffer from intrinsic limitations, including system complexity, response lag, and susceptibility to external disturbances.

While PCT testing can estimate the SOH by tracking variations in pressure, temperature, and hydrogen concentration, it lacks the capability for *in situ* or real-time monitoring, with measurement results often subject to significant feedback delays [32–34]. This limitation becomes especially critical during the dynamic cycling of hydrogen storage materials,

* These authors contributed equally to this work.
✉ Corresponding authors: Weijie Yang E-mail: yangwj@ncepu.edu.cn; Juan Chen E-mail: juanchen@sjtu.edu.cn

where environmental fluctuations can compromise data accuracy and introduce substantial deviations [35]. In contrast, mass flow meters allow real-time hydrogen flow monitoring and indirectly reflect SOH variations. However, their performance degrades over repeated cycling, resulting in increased measurement errors and reduced reliability [36]. Additionally, the deployment of mass flow meters adds to system complexity and incurs higher installation and maintenance costs. Collectively, these shortcomings highlight the inadequacy of current SOH detection techniques in delivering real-time, precise, and cost-effective monitoring, underscoring the pressing need for the development of more advanced and efficient detection methods.

To address the challenge of real-time SOH monitoring in solid-state hydrogen storage systems, this study proposes an optical detection strategy based on the hydrogenochromism effect [37]. This phenomenon describes the pronounced changes in optical properties of certain metal hydrides, such as magnesium hydride (MgH_2), when exposed to hydrogen [38]. Specifically, under hydrogen-rich conditions, magnesium films transition from a reflective metallic state to a transparent dielectric state [39]. This transformation is strongly correlated with modifications in the electronic structure, bandgap, and free electron concentration of the material. By performing continuous measurements of key optical parameters such as reflectance, extinction coefficient, absorption coefficient, energy loss spectrum, and refractive index, it becomes possible to monitor the hydrogen absorption and desorption processes in real time and dynamically estimate the SOH.

Compared with conventional SOH detection methods, the hydrogenochromism-based optical approach offers several distinct advantages. First, it enables *in situ* and real-time monitoring without necessitating structural modifications to the hydrogen storage system, thereby ensuring operational simplicity and cost efficiency. Second, the method exhibits high sensitivity, capable of capturing subtle variations in hydrogen content, which facilitates more accurate SOH assessment. Notably, at specific wavelengths within the infrared, visible, and ultraviolet regions, the reflectance and refractive index of MgH_2 exhibit strong linear correlations with SOH, providing a robust theoretical basis for practical implementation. Furthermore, the optical strategy demonstrates broad applicability, extending beyond MgH_2 to encompass a wide range of metal hydrides and hydrogen storage materials, highlighting its potential for widespread adoption in next-generation hydrogen technologies.

Density functional theory (DFT) has established itself as a powerful and reliable computational tool for probing the hydrogen storage properties of MgH_2 [40–45]. By accurately modeling the electronic structure and simulating the response of the material under various hydrogenation states, DFT facilitates the prediction of hydrogen adsorption/desorption dynamics, reaction pathways, and associated structural and energetic changes. These atomistic insights are instrumental in elucidating the underlying hydrogen storage mechanisms and guiding the design and optimization of Mg-based hydrogen storage systems. With its combination of high accuracy and favorable computational efficiency, DFT is particularly well-suited for atomic-scale investigations of solid-state hydrogen storage materials [46].

Although DFT provides valuable insights into the optical properties of hydrogen storage materials, theoretical predictions alone cannot fully capture the complexities of real-world systems. To enhance the reliability and practical relevance of the simulation results, a complementary experimental investigation is also essential. In this work, reflectance at 940 nm, a near-infrared wavelength identified through theoretical sensitivity analysis, was monitored during hydrogenation. This qualitative agreement supports the correlation between infrared reflectance and the hydrogenation state of Mg-based thin films under the tested conditions.

This work employs DFT calculations to investigate the variation in the optical properties of MgH_2 under different hydrogenation states. The results demonstrate a strong linear correlation between SOH and key optical parameters, including reflectance and refractive index, thus providing a robust theoretical foundation for real-time SOH monitoring. To validate the theoretical predictions, reflectance measurements were conducted at 940 nm, a near-infrared wavelength selected based on its high sensitivity to hydrogenation as identified through simulation. The experimental results exhibit a consistent trend with the theoretical model, showing decreased reflectance with increasing hydrogen uptake, which supports the reliability and applicability of the proposed method. Leveraging the hydrogenochromism effect, this optical detection approach overcomes the limitations of conventional SOH diagnostic techniques by enabling real-time, non-invasive monitoring without the need for complex instrumentation. This integrated theoretical–experimental strategy not only enhances the feasibility of SOH tracking in practical applications but also opens new avenues for the development of intelligent, optically responsive hydrogen storage systems. With its high scalability and compatibility, the method holds strong promise for widespread deployment in the hydrogen energy sector, thereby supporting the commercialization of solid-state hydrogen storage technologies and contributing to the sustainable advancement of the global hydrogen economy.

2. Theoretical and experimental methods

2.1. Structure

Under the MgH_2 structure with the lowest formation energy, the unit cell is expanded by a factor of 2, 2, and 3 in the *x*, *y*, and *z* directions, respectively, resulting in a final supercell of $Mg_{24}H_{48}$, as shown in Fig. 1(a). The CONTCAR file of the structure at 100% SOH is provided in Table S1, while the optimized structures of MgH_2 at different SOH values are shown in Fig. S1. It is noted that the structures undergo certain modifications after optimization at different hydrogen contents; however, the overall framework remains preserved. Based on this structure, hydrogen atoms are randomly de-

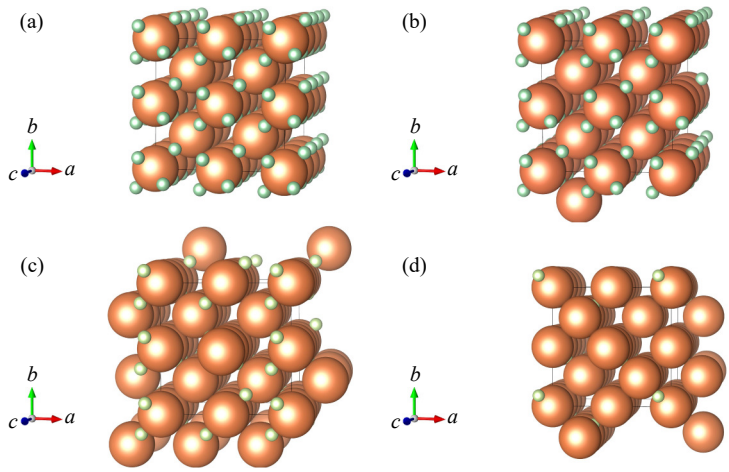

Fig. 1. MgH_2 structures under different SOH levels: (a) 100%; (b) 70%; (c) 40%; (d) 10%. Orange spheres represent Mg, and green spheres represent H.

leted in intervals corresponding to 10% of the hydrogen atom count, simulating the dehydrogenation process until no hydrogen atoms remain, leaving pure magnesium metal. Since the dehydrogenation mechanism of MgH_2 has not been definitively validated theoretically, three different structures were used for calculations at each different SOH state to ensure the relative accuracy of the results. Specifically, in each structure, hydrogen atoms are randomly deleted in three distinct ways until the final hydrogen atom count is consistent. Fig. 1(b)–(d) shows the MgH_2 structures at 70%, 40%, and 10% SOH, respectively. An error analysis is performed on the calculation results for these three structures, producing a data plot with the SOH on the *x*-axis and the corresponding optical properties on the *y*-axis. To ensure that the computed optical properties reflect stable and physically meaningful configurations, all MgH_2 structures with different SOH values were fully relaxed prior to property calculations, thereby minimizing the impact of vacancy defects introduced during dehydrogenation.

2.2. DFT Calculation

DFT calculations are widely utilized for predicting and exploring material properties, owing to their efficiency, accuracy, and relatively low computational cost [47–49]. In this study, all simulations were carried out using the Vienna *ab initio* simulation package (VASP) along with the projector augmented wave (PAW) method [50]. The exchange-correlation interactions were handled by the generalized gradient approximation (GGA) and the Perdew–Burke–Ernzerhof (PBE) functional [51]. Considering the spin-polarized electronic structure of magnesium hydride (MgH_2), a spin polarization was applied (ISPIN = 2) [52]. The electron energy levels were populated using Gaussian smearing with a width of σ = 0.05 eV. To optimize computational efficiency while maintaining accuracy, various *k*-point meshes were tested, as illustrated in Fig. S2. The geometry of the system was first optimized using a 2 × 2 × 2 Γ-centered *k*-point mesh, with an energy cutoff of 450 eV and a force convergence threshold of 0.01 eV/Å for each atom, where Γ denotes the center of the Brillouin zone ($k = 0$). For the subsequent electronic self-consistent calculations, the same *k*-point grid was adopted, with a convergence criterion of 1×10^{-5} eV. In the optical property calculations, the number of bands was chosen to be approximately twice the number of occupied bands, providing sufficient unoccupied states to accurately describe the interband transitions, particularly in the high-energy (ultraviolet) region.

After the calculations are completed, the optical properties of the material are obtained using the Vaspkit toolkit from the raw data calculated using the VASP code [53]. The linear optical properties can be obtained from the frequency-dependent complex dielectric function $\varepsilon(\omega)$:

$$\varepsilon(\omega) = \varepsilon_1(\omega) + \mathrm{i}\varepsilon_2(\omega) \tag{1}$$

where $\varepsilon_1(\omega)$ and $\varepsilon_2(\omega)$ are the real and imaginary parts of the dielectric function, and ω is the photon frequency.

The frequency-dependent linear optical spectra, e.g., reflectance $n(\omega)$, extinction coefficient $\kappa(\omega)$, absorption coefficient $\alpha(\omega)$, energy-loss function $L(\omega)$, and refractive index $R(\omega)$ can be calculated from the real $\varepsilon_1(\omega)$ and the imaginary $\varepsilon_2(\omega)$ parts [54]:

$$n(\omega) = \left[\frac{\sqrt{\varepsilon_1^2(\omega)+\varepsilon_2^2(\omega)}+\varepsilon_1(\omega)}{2}\right]^{\frac{1}{2}} \tag{2}$$

$$\kappa(\omega) = \left[\frac{\sqrt{\varepsilon_1^2(\omega)+\varepsilon_2^2(\omega)}-\varepsilon_1(\omega)}{2}\right]^{\frac{1}{2}} \tag{3}$$

$$\alpha(\omega) = \frac{\sqrt{2}\omega}{c}\left[\sqrt{\varepsilon_1(\omega)^2+\varepsilon_2(\omega)^2}-\varepsilon_1(\omega)\right]^{\frac{1}{2}} \tag{4}$$

$$L(\omega) = \mathrm{Im}\left(\frac{-1}{\varepsilon(\omega)}\right) = \frac{\varepsilon_2(\omega)}{\varepsilon_1^2(\omega)+\varepsilon_2^2(\omega)} \tag{5}$$

$$R(\omega) = \frac{[n(\omega)-1]^2+\kappa^2(\omega)}{[n(\omega)+1]^2+\kappa^2(\omega)} \tag{6}$$

where c is the speed of light in vacuum, Im denotes the imaginary part of a complex function. In this study, the frequency-dependent dielectric functions of MgH_2 were com-

puted along the principal crystallographic directions to account for its intrinsic anisotropy. For clarity, the results are predominantly presented as a function of wavelength λ (nm), while photon energy E (eV) is also referenced where appropriate. The conversion between photon energy and wavelength follows the relation:

$$E = \frac{1240}{\lambda} \quad (7)$$

For clarity, the spectral regions are categorized as infrared (0–1.65 eV, corresponding to wavelengths > 700 nm), visible (1.65–3.1 eV, 700–400 nm), and ultraviolet (>3.1 eV, <400 nm). This dual representation ensures consistency with conventional practice in optical studies and provides a clearer physical interpretation of the results.

It should be noted that the data presented in this work are the processed results after applying linear interpolation, which was performed to smooth the curves and facilitate subsequent analysis and summary. All raw (unprocessed) data are openly available in a public GitHub repository (https://github.com/Weijie-Yang/DFT-Optics-Data) for reference and further analysis.

2.3. Experimental methods

The following steps were taken in the experimental procedure.

(1) Sample preparation. Pd/Mg bilayer thin films were deposited onto quartz glass substrates with a diameter of 37 mm using direct current (DC) magnetron sputtering. The base pressure was maintained at 1×10^{-6} Torr, and high-purity argon gas was introduced at a flow rate of 5.0×10^{-7} m^3/s as the working gas. Prior to deposition, both Mg and Pd targets were pre-sputtered for 30 s to remove possible surface contaminants. The Mg layer was deposited using a DC power of 40 W for 120 s, followed by the deposition of the Pd layer at 80 W for 25 s. The Pd overlayer acts as a catalytic layer to enhance hydrogen dissociation and absorption into the underlying Mg film.

(2) Optical measurements. The hydrogen-induced optical response of the thin films was evaluated using a spectrophotometer (Hitachi UH-4150). In the experiment, reflectance was monitored at 940 nm. This near-infrared wavelength was strategically selected based on a combination of theoretical sensitivity and practical advantages. Our simulations confirmed that this spectral region exhibits a monotonic reflectance response to hydrogenation. Furthermore, the 940 nm wavelength is particularly advantageous for sensor development due to the wide availability of low-cost and reliable light sources and detectors, making it ideal for the future engineering of portable and affordable devices. Real-time reflectance measurements were recorded using a spectrophotometer with a probe beam diameter of approximately 3 mm. This large spot size ensures the measurement is a macroscopic average of the film's optical properties.

To enable dynamic hydrogenation experiments, a gas mixing and flow control system was integrated with the measurement chamber. The films were exposed to a synthetic air atmosphere with hydrogen concentrations alternating between 0.25vol% and 0.5vol%. These specific concentrations were determined based on preliminary characterization of the film's optical response. The 0.25vol% H_2 concentration was chosen as it corresponds to a stable reflectance plateau, indicating a quasi-equilibrium state suitable for establishing a reproducible baseline. Subsequently, the concentration was increased to 0.5vol% H_2 to drive the system into a distinct and measurable response regime, characterized by a monotonic decrease in reflectance. This stepped approach, alternating between a stable plateau and a controlled descent, allows for a clear and systematic investigation of the film's dynamic response to changes in hydrogen concentration.

The total gas flow rate was maintained at 1.67×10^{-6} m^3/s under a constant pressure of 0.1 MPa. Real-time reflectance spectra were recorded to monitor the optical changes as a function of hydrogen exposure. Synthetic air was used as the carrier gas. This is a critical choice, as the presence of oxygen creates a dynamic balance between hydrogen absorption and desorption on the catalyst surface, allowing the film to stabilize at a controllable, intermediate state of hydrogenation. This condition is challenging to achieve in an inert H_2/Ar atmosphere.

(3) Scanning electron microscope (SEM) and energy dispersive spectroscopy (EDS) characterization. The surface morphology and elemental composition of the thin films were characterized using an SEM (Helios 5 CX) equipped with an EDS system. SEM imaging was performed at an accelerating voltage of 5 keV with a beam current of 0.17 nA, while EDS mapping was conducted at 20 keV and 11 nA to acquire compositional information.

3. Results and discussion

3.1. Optical properties at different SOH levels

To investigate the feasibility of employing optical properties for non-invasive SOH detection in Mg-based hydrogen storage materials, we systematically analyzed the variation of four key optical parameters: reflectance, extinction coefficient, absorption coefficient, and refractive index, across the infrared, visible, and ultraviolet spectral ranges. All results were derived from first-principles calculations, with characteristic variation trends illustrated in Fig. 2. The complete spectral datasets corresponding to different hydrogenation states are provided in the Supporting Information, as shown in Figs. S3–S7.

Reflectance exhibits a clear and monotonic dependence on SOH across both the infrared and visible regions. As shown in Fig. 2(a), reflectance increases uniformly with decreasing SOH in the infrared range. A similar pattern is observed in the visible range, as shown in Fig. 2(b). Furthermore, for each SOH level, reflectance remains largely invariant with wavelength across both regions, indicating excellent spectral stability. This combination of monotonicity and low wavelength sensitivity makes reflectance a highly promising candidate for practical SOH detection, especially at selected near-infrared or visible wavelengths.

The extinction coefficient shows a generally increasing

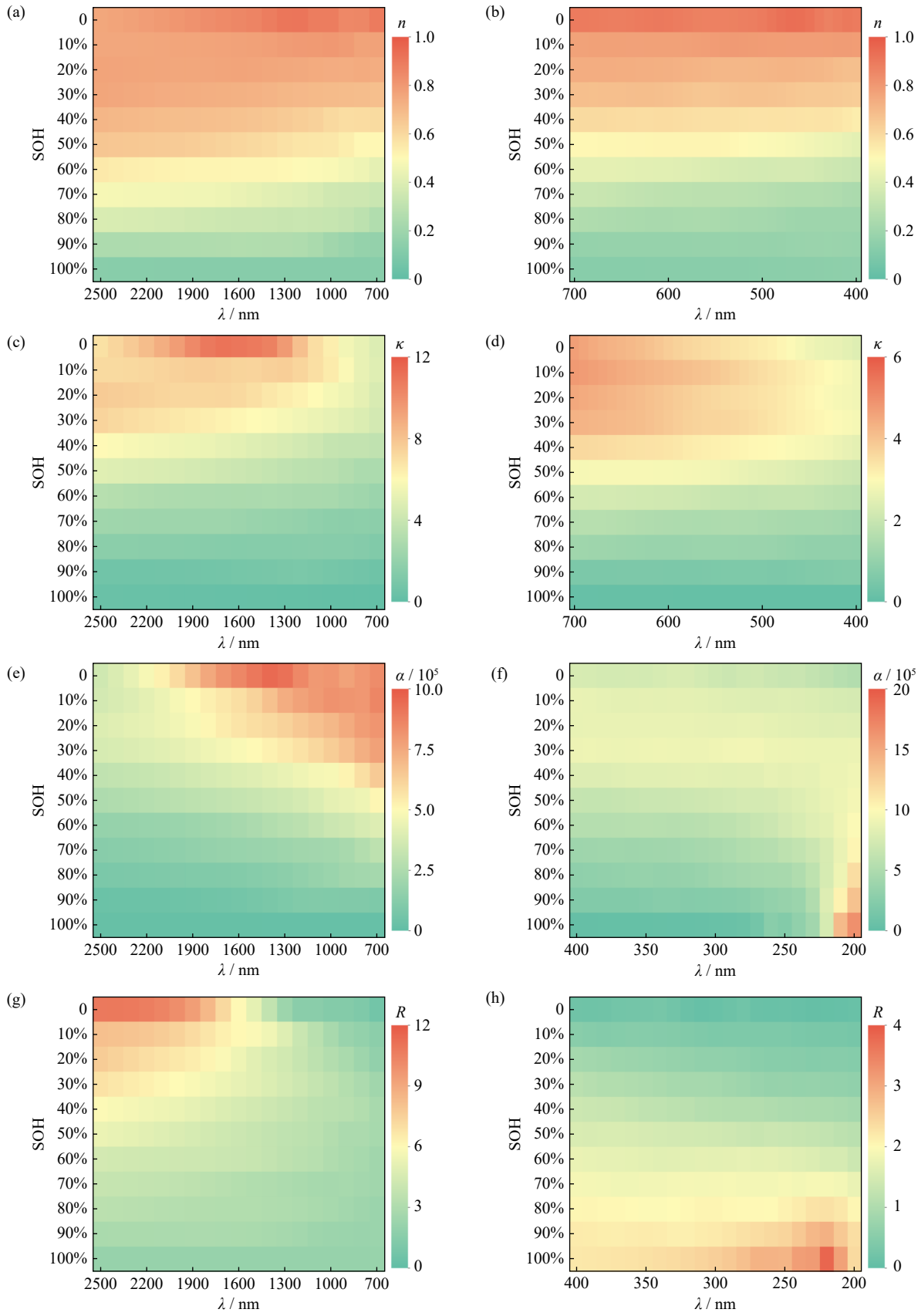

Fig. 2. Optical properties of MgH_2 as a function of wavelength and SOH: (a) infrared reflectance, (b) visible reflectance, (c) infrared extinction coefficient, (d) visible extinction coefficient, (e) infrared absorption coefficient, (f) ultraviolet absorption coefficient, (g) infrared refractive index, and (h) ultraviolet refractive index.

trend with decreasing SOH, particularly in the infrared range, where more significant changes are observed between 1200 and 2300 nm, as shown in Fig. 2(c). In the visible range, this trend largely holds, except at SOH = 0 (pure Mg), where a

slight decrease occurs, likely due to the absence of hydrogen, as shown in Fig. 2(d). However, unlike reflectance, the extinction coefficient exhibits relatively poor monotonicity when the SOH falls below approximately 30% and less consistent variation with wavelength. These irregularities, especially in the low-SOH regime, suggest that while the extinction coefficient reflects underlying optical transitions, its application in reliable SOH quantification may be limited due to its non-uniform spectral response.

The absorption coefficient behaves similarly. In the infrared region, it increases with decreasing SOH, especially in the 700–2000 nm range, indicating enhanced absorption as hydrogen is released, as shown in Fig. 2(e). However, in the ultraviolet range, the response becomes more complex: in the 200–250 nm region, absorption decreases with decreasing SOH, whereas from 250 to 400 nm it increases, as shown in Fig. 2(f). This crossover behavior reflects competing electronic transitions and suggests that the absorption coefficient is sensitive to subtle changes in band structure. Nevertheless, the inconsistent monotonicity and increased wavelength dependence, especially at the spectral edges, reduce its suitability as a standalone SOH indicator in practical sensing applications.

In contrast, the refractive index demonstrates a more stable and predictable response to SOH. As shown in Fig. 2(g), in the infrared region (1600–2500 nm), it increases consistently as SOH decreases. In the ultraviolet region, as shown in Fig. 2(h), the refractive index shows a steady decrease with decreasing SOH, particularly pronounced in the 200–300 nm range. Across both spectral regions, the refractive index generally exhibits low sensitivity to wavelength; however, enhanced sensitivity is observed in the infrared region at low SOH values and in the ultraviolet region at high SOH values, suggesting that it is also a robust indicator for hydrogenation level. Its smooth variation and spectral stability make it a promising complement to reflectance in the development of optical SOH sensing methods.

3.2. Linear fitting of optical properties and SOH correlation

The four optical properties discussed above exhibit a monotonic relationship with SOH in certain wavelength ranges across different regions of the electromagnetic spectrum. To further investigate these relationships, representative wavelengths were selected for detailed analysis. Specifically, the reflectance was analyzed at 1200 nm and 550 nm, the extinction coefficient at 1200 nm and 600 nm, the absorption coefficient at 1200 nm and 200 nm, and the refractive index at 1700 nm and 250 nm. The results of the linear fittings of these optical properties as a function of SOH at these selected wavelengths are shown in Fig. 3.

To verify the validity of the functions between the optical properties and SOH, optical data for SOH values of 96%, 84%, 75%, 66%, 57%, 45%, 33%, 24%, 12%, and 6% were calculated for validation. The results of the mean absolute error (MAE) are shown for these random data in Fig. 4(a). Detailed MAE values for each case are provided in the Tables S2–S9.

These results indicate that the reflectance exhibits the best linear fit in both the infrared and visible light ranges. Specifically, in the infrared (1200 nm) and visible light (550 nm) ranges, the coefficient of determination (r^2) for reflectance are both 0.99, with a MAE approximately 5%. These findings demonstrate a strong linear relationship between reflectance and SOH at these two wavelengths, establishing reflectance as a reliable indicator for SOH monitoring. Furthermore, the optical data fitting results for these two ranges are stable and accurate, further validating the reliability of reflectance in real-time SOH monitoring.

On the other hand, although the absorption and extinction coefficients show some degree of linearity within certain wavelength ranges, their fit quality is clearly inferior to that of reflectance. In the infrared range, the r^2 values for the absorption and extinction coefficients are relatively high, at 0.99 for both, but in the visible light range, particularly at 600 nm, the r^2 value for the extinction coefficient drops to 0.93, and the increase in MAE suggests that the optical response at shorter wavelengths is more complex and may be affected by additional factors. Therefore, despite the potential application value of the absorption and extinction coefficients under certain conditions, their weaker linear fitting relative to reflectance limits their broader utility in SOH monitoring.

Finally, the refractive index in the ultraviolet range (250 nm) demonstrates a high r^2 value (0.99) and low error (MAE of 0.04) during the fitting process, indicating a strong linear relationship between refractive index and SOH in the ultraviolet range with excellent fitting accuracy.

Fig. 4(b)–(d) respectively illustrates the distributions of the fitted linear relationships between the SOH and the reflectance at 1200 nm and 550 nm based on random data points, as well as the distribution of the fitted linear relationship between the SOH and the refractive index at 250 nm derived from random data. The distributions of the fitted linear relationships between the SOH and various optical properties at different wavelengths, based on randomly selected data points, are presented in Figs. S8–S12.

The above results indicate that the applicability of the linear model depends on the theoretical coupling mechanisms between the spectral range and parameter combinations. For parameters such as reflectance and refractive index, their linear relationship with SOH is theoretically valid within specific wavelength ranges. However, the relationship for parameters like extinction coefficient and absorption coefficient requires extension to nonlinear or multivariate theoretical models. A comprehensive analysis reveals that reflectance in the infrared range and in the visible light range and refractive index in the ultraviolet range are the most suitable optical properties for SOH monitoring, with their superior linear fit and low error making them powerful tools for future hydrogen state detection.

3.3. Electronic structure origin of optical responses

From an electronic structure perspective, Mg is a typical

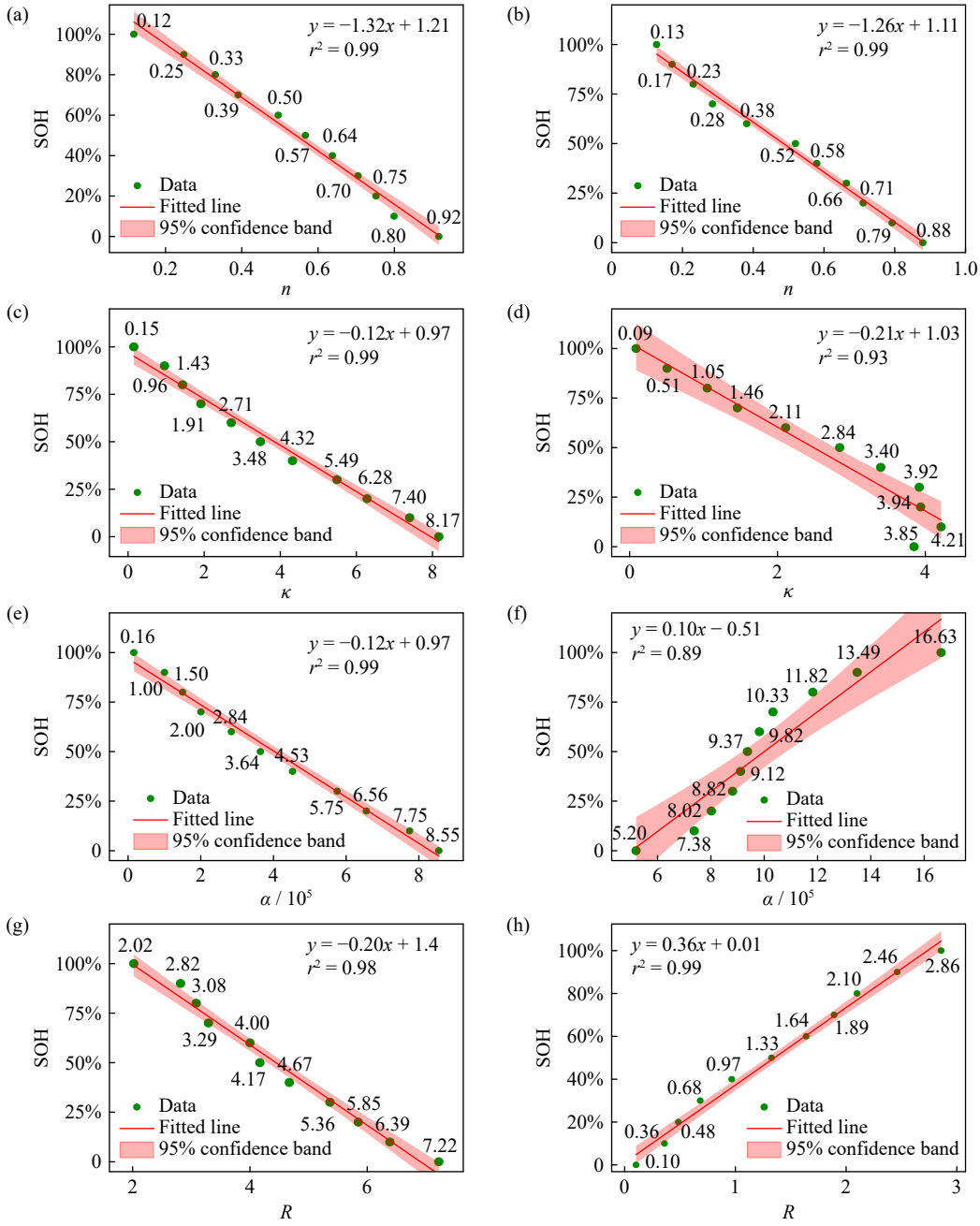

Fig. 3. Linear fitting of MgH_2 optical properties with SOH: (a) infrared reflectance, (b) visible reflectance, (c) infrared extinction coefficient, (d) visible extinction coefficient, (e) infrared absorption coefficient, (f) ultraviolet absorption coefficient, (g) infrared refractive index, and (h) ultraviolet refractive index.

metal characterized by overlapping conduction and valence bands (bandgap of 0 eV) and exhibits extremely high free electron concentration. While optical properties can also be influenced by lattice and nuclear contributions, the present analysis focuses on the electronic structure, which accounts for the dominant features of the high reflectance and low transmittance observed across the visible to infrared spectral range, consistent with the typical optical response of metals. Upon the reaction of Mg with H_2 to form MgH_2, the crystal structure undergoes a transition from hexagonal close-packed to tetragonal, accompanied by an electronic redistribution that results in a significant bandgap enlargement to approximately 5.6 eV, which aligns well with previously reported experimental values ((5.6 ± 0.1) eV) [55]. This wide bandgap prevents visible light (energy range of approximately 1.65–3.1 eV) from exciting electronic transitions, consequently rendering MgH_2 transparent in the visible spectrum with reduced reflectance.

Fig. 5 presents the density of states (DOS) plots corresponding to SOH values of 100%, 80%, 60%, 40%, 20%, and 0. This study focuses on optical properties, and thus, the electronic energy is examined within the 0–7 eV range. It is evident that, within the infrared and visible light regions, as SOH decreases, the DOS curves become steeper, and the absorption peaks within this energy range become more pronounced, resulting in enhanced light absorption and a subsequent increase in reflectance. In the near-ultraviolet range, the DOS curves also exhibit a steeper trend with decreasing

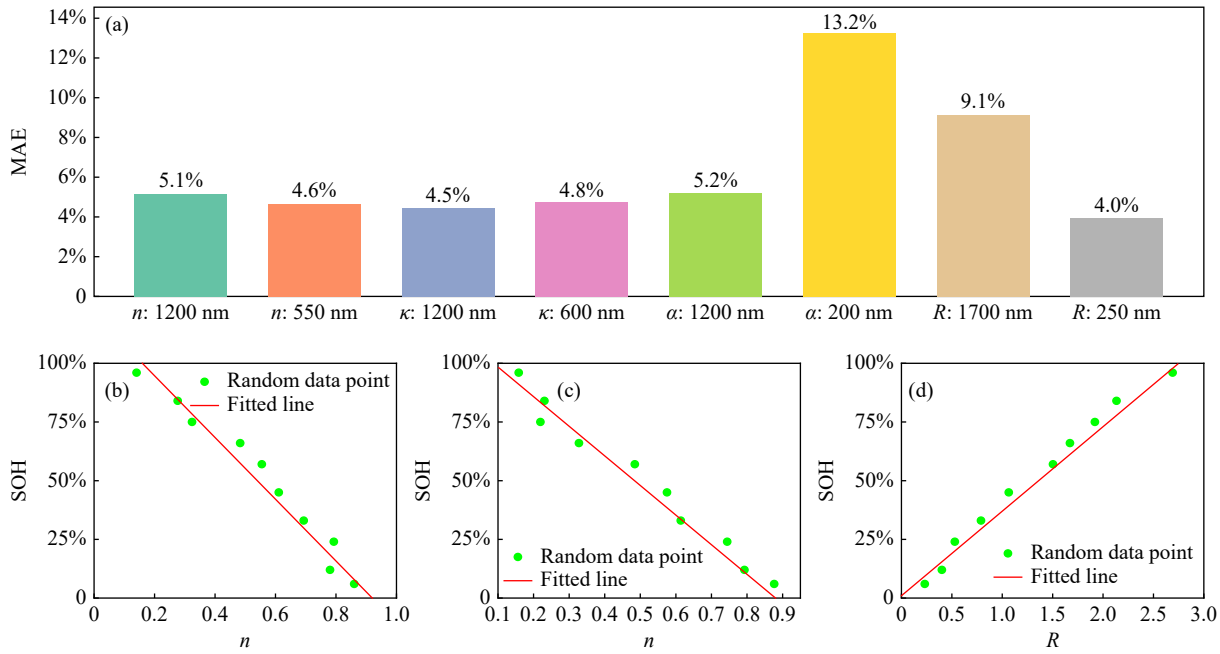

Fig. 4. (a) Results of the mean absolute error, (b) randomly sampled reflectance data at 1200 nm fitted with a linear regression as a function of the SOH, (c) randomly sampled reflectance data at 550 nm fitted with a linear regression as a function of the SOH, and (d) randomly sampled refractive index data at 250 nm fitted with a linear regression as a function of the SOH.

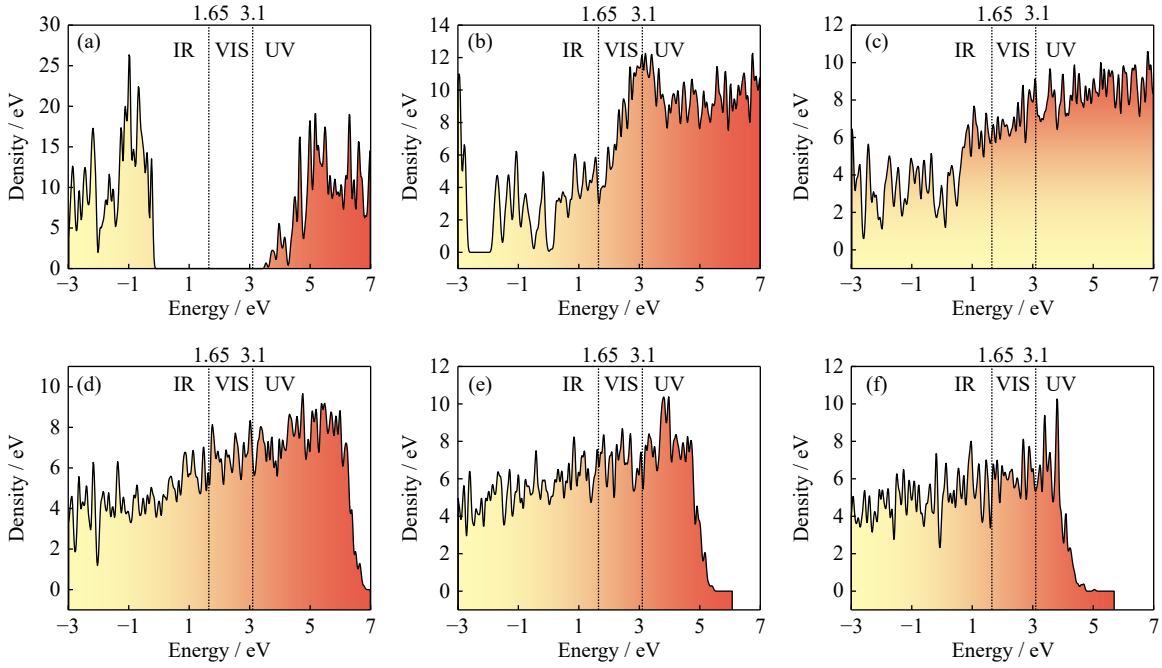

Fig. 5. DOS curves at different SOH values: (a) 100%, (b) 80%, (c) 60%, (d) 40%, (e) 20%, and (f) 0 (1.65 eV is the infrared–visible boundary; 3.1 eV is the visible–ultraviolet boundary; IR, VIS, and UV represent the infrared, visible, and ultraviolet regions, respectively).

SOH, indicating an increased absorption of ultraviolet light by MgH_2, which slows the propagation speed of light and thereby decreases the refractive index.

From the perspective of dielectric constant analysis, based on the Drude model, the complex dielectric constant $\varepsilon(\omega)$ of the material can be expressed as [56]:

$$\varepsilon(\omega) = 1 - \frac{Ne^2}{[\varepsilon_0 m(\omega^2 + \mathrm{i}\gamma\omega)]} \tag{8}$$

where N represents the free electron concentration, e denotes the electron charge, m signifies the electron mass, and γ indicates the electron scattering rate, and ε_0 denotes the permittivity of free space. For Mg, the negative real part of its dielectric constant with a substantially larger imaginary part is attributed to its high free electron concentration, which inherently exhibits metallic behavior. Meanwhile, the free electron concentration of MgH_2 decreases drastically (N reduced by approximately two orders of magnitude), and the simultaneous 30% volume expansion further dilutes the electron

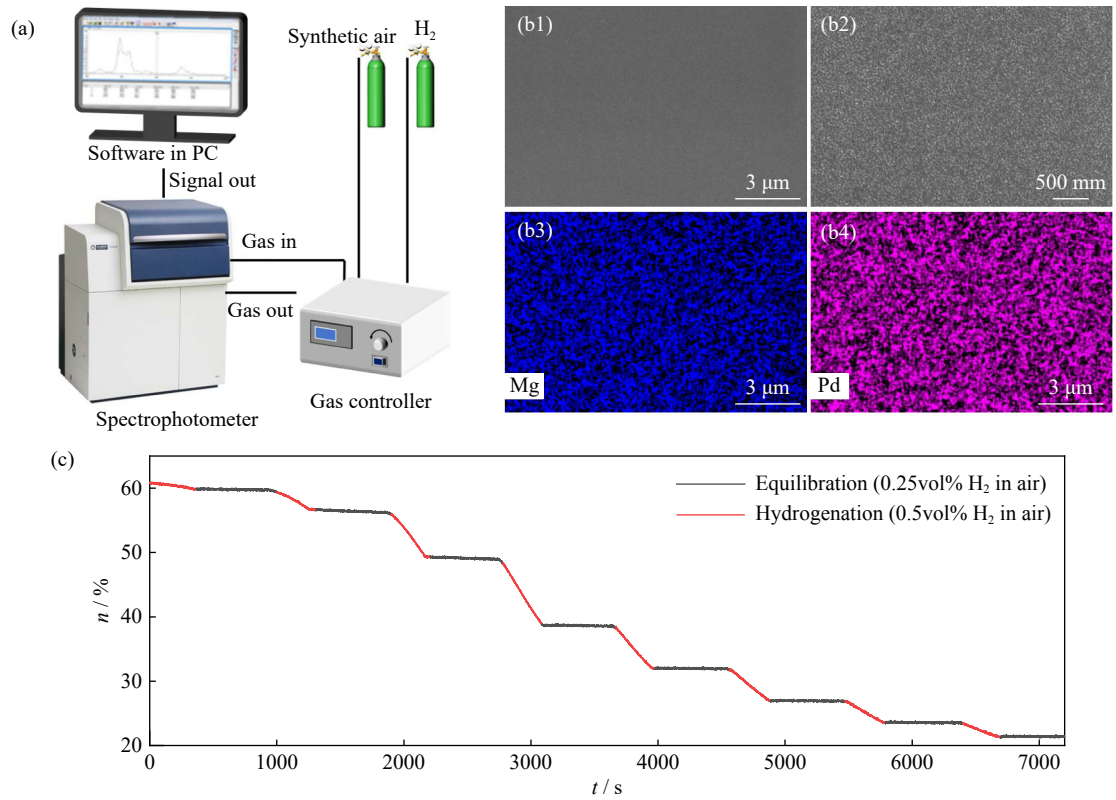

Fig. 6. (a) Schematic of the experimental setup for *in situ* reflectance measurement under controlled hydrogen concentrations. (b1, b2) SEM images at 30000× (b1) and 100000× (b2) magnifications showing the surface morphology of the Pd/Mg film; (b3, b4) EDS elemental mapping confirming uniform distribution of (b3) Mg and (b4) Pd. (c) Reflectance (*n*) vs. time (*t*) plot during alternating gas exposure.

density. This dual effect causes the real part of the dielectric constant to increase significantly (approaching insulator levels) while the imaginary part approaches zero, thereby inducing a substantial reduction in reflectance.

3.4. Experimental validation of theoretical predictions

To further validate the reliability of the theoretical predictions, experimental investigations were conducted. A schematic of the experimental system used to measure the hydrogen-induced optical response is shown in Fig. 6(a). This setup enables *in situ* reflectance monitoring of the Pd/Mg film during alternating exposure to hydrogen-enriched synthetic air with precisely controlled concentrations. Gas flow is directed across the sample surface, and reflectance is recorded in real time, allowing step-resolved analysis of hydrogenation dynamics under varying ambient conditions.

Fig. 6(b) presents the SEM and EDS characterization of the deposited thin films. At 30000× magnification, the film surface appears smooth and lacks distinctive morphological features, indicating uniform deposition. When observed at a higher magnification of 100000×, fine-scale topographical texture becomes visible without evidence of cracking or delamination. This suggests that the bilayer film maintains a dense and continuous morphology across different length scales. In addition, EDS elemental mapping confirms that both Pd and Mg are uniformly distributed over the surface, with no signs of aggregation. Collectively, these images and maps confirm the high degree of morphological and compositional uniformity of the prepared films. This uniformity is critical as it ensures that the optical measurements are reliable and representative of the entire film, rather than being skewed by local inconsistencies.

The real-time optical response of the film under alternating hydrogen concentrations is shown in Fig. 6(c), where $\%n$ represents the reflectance and t denotes the experimental time. It is important to note that the comparison between the DFT model (pure Mg) and our experimental data (Pd/Mg) is qualitative. The analysis focuses on validating the trend of reflectance change, as the measured absolute values are influenced by the Pd capping layer. The observed decrease in reflectance upon hydrogenation is dominated by the metal-to-semiconductor phase transition of the 40 nm Mg layer, while the optical contribution from the very thin (5 nm) Pd layer is treated as a quasi-static background. The excellent agreement in this trend provides strong validation for our theoretical model. A clear stepwise decrease in reflectance is observed as the sample is alternately exposed to 0.25vol% and 0.5vol% H_2 in synthetic air. Each exposure cycle results in a rapid transition followed by a stable plateau, indicating fast hydrogen uptake and subsequent stabilization at a given hydrogenation level. These plateaus suggest that the film reaches a quasi-steady internal hydrogenation level, corresponding to the specific ambient hydrogen conditions. This sensitivity to small differences in environmental hydrogen concentration is reflected in the optical response and shows qualitative agreement with the simulation results. In the the-

oretical model, the reflectance of the material was predicted to vary with the SOH, which represents the hydrogen content within the film, particularly in the infrared region. It is noteworthy that the film exhibits a rapid and fully reversible response upon cycling the hydrogen concentration. This behavior provides strong experimental evidence that significant, performance-degrading oxidation of the Mg film is not occurring, as such effects would typically manifest as a sluggish response, a drifting baseline, or incomplete recovery.

In the experiment, reflectance was monitored at 940 nm, a near-infrared wavelength selected based on its theoretically predicted sensitivity to hydrogenation. The measured reflectance decreases with increasing hydrogen uptake by the film, which is consistent with the simulation trend where reflectance increases as SOH decreases. Although the SOH in the simulation is defined by the hydrogen content in the material, and the experiment controls the hydrogen concentration in the ambient atmosphere, the observed optical response follows the same qualitative direction. This agreement between simulation and experiment supports the correlation between infrared reflectance and the hydrogenation state of Mg-based thin films under the tested conditions.

3.5. Conceptual framework for optical SOH detection

The distinct optical responses of Mg and MgH_2 primarily arise from their fundamental differences in electronic structure and free electron concentration. Metallic Mg exhibits high reflectance due to its abundant free electrons, while MgH_2 becomes optically transparent as a result of its wide bandgap and significantly reduced carrier density. Based on these characteristics, our theoretical calculations established clear linear correlations between both reflectance and refractive index with the SOH. In the experimental verification, reflectance measurements were performed at a wavelength selected for its high sensitivity, and the observed trend showed good agreement with the theoretical prediction. Although the refractive index was not directly measured in this study, the underlying theoretical framework remains applicable and consistent. Fig. 7 illustrates a schematic concept for SOH detection in MgH_2 using optical methods. A light source directs an incident beam onto the sample, with both reflected and refracted components captured by detectors. Variations in reflectance and refractive index, which are theoretically associated with the SOH, are monitored simultaneously. The relationships between these optical properties and SOH are shown in Fig. 4(b)–(d), revealing clear linear correlations and their potential for quantitative analysis.

4. Conclusion

As global energy transitions accelerate, hydrogen energy is increasingly regarded as a cornerstone of sustainable infrastructure. In this study, we systematically evaluated the optical properties of MgH_2 across the infrared, visible, and ultraviolet spectral regions, and identified robust linear correlations between SOH and specific parameters, such as reflectance at 1200 nm and 550 nm and refractive index at 250 nm ($r^2 \geq 0.99$). These findings provide a solid theoretical foundation for non-invasive, real-time SOH diagnostics in solid-state hydrogen storage. The reliability of this approach was further supported by experimental reflectance measurements in the near-infrared range, which exhibited consistent agreement with theoretical predictions and demonstrated the importance of integrating first-principles calculations with experimental validation. Beyond establishing fundamental correlations, this work also highlights the potential of optical sensing as a practical strategy for hydrogen storage monitoring, offering new insights into the design of intelligent, spectroscopically responsive systems. Nevertheless, practical implementation will require overcoming challenges related to environmental signal interference, material stability under cyclic operation, and sensor integration into compact architectures. As a key step toward practical application, establishing precise quantitative calibration to directly correlate optical signals with absolute hydrogen content will be essential. Integrating optical measurements with *in-situ* mass-sensitive techniques, such as quartz crystal microbalance (QCM), offers a promising pathway to develop robust models linking reflectance to SOH. Addressing these challenges, alongside advancing device-level integration and *in-situ* testing, will be essential to bridge the gap between laboratory demonstrations and industrial deployment, ultimately contributing to

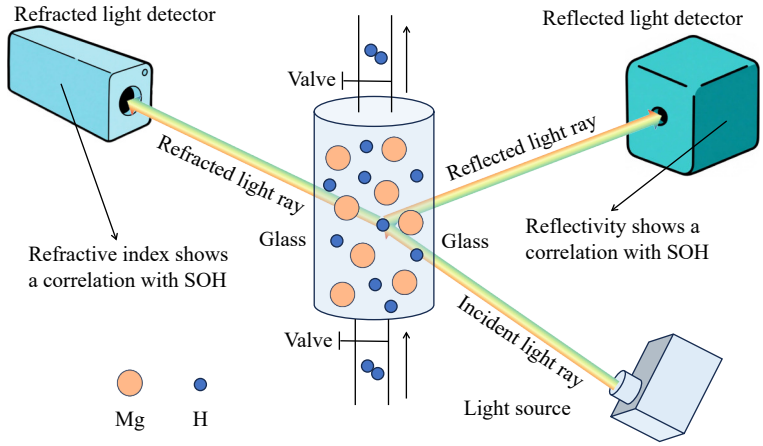

Fig. 7. Schematic diagram of the reflectance and refractive index measurement.

safer, more efficient, and sustainable hydrogen-based energy systems.

Acknowledgements

This work was funded by the Natural Science Foundation of Hebei Province, China (No. E2023502006) and the Fundamental Research Fund for the Central Universities, China (No. 2025MS131).

Conflict of Interest

The authors declare no conflict of interest.

Supplementary Information

The online version contains supplementary material available at https://doi.org/10.1007/s12613-025-3284-6. All raw data used in this study, which are openly accessible through a public GitHub repository (https://github.com/Weijie-Yang/DFT-Optics-Data).

References

[1] F.Q. Bu, A. Wajid, M.Y. Gu, *et al*., Synergistic effect of multivalent Ti, Zr, and oxygen vacancies to significantly enhance the hydrogen sorption properties of MgH_2, *J. Mater. Chem. A*, 13(2025), No. 21, p. 16102.

[2] A. Kovač, M. Paranos, and D. Marciuš, Hydrogen in energy transition: A review, *Int. J. Hydrogen Energy*, 46(2021), No. 16, p. 10016.

[3] Z.L. Yuan, X.X. Zhang, Y.T. Wu, *et al*., Effectively enhanced catalytic effect of sulfur doped Ti_3C_2 on the kinetics and cyclic stability of hydrogen storage in MgH_2, *J. Magnesium Alloys*, 13(2025), No. 4, p. 1843.

[4] Y.Y. Zhao, Z.B. Liu, J.C. Liu, *et al*., Improvement effect of reversible solid solutions $Mg_2Ni(Cu)/Mg_2Ni(Cu)H_4$ on hydrogen storage performance of MgH_2, *J. Magnesium Alloys*, 12(2024), No. 1, p. 197.

[5] T.A. Yao, Y. Yang, J.H. Cai, *et al*., From LLM to Agent: A large-language-model-driven machine learning framework for catalyst design of MgH_2 dehydrogenation, *J. Magnesium Alloys*, (2025).

[6] J.H. Cai, H.B. Wang, X.T. Tang, *et al*., Data-driven evidence for the burst effect in MgH_2 dehydrogenation via analysis of experimental kinetic curves, *J. Energy Storage*, 136(2025), art. No. 118450.

[7] L. Peraldo Bicelli, Hydrogen: A clean energy source, *Int. J. Hydrogen Energy*, 11(1986), No. 9, p. 555.

[8] I. Darmadi, F.A.A. Nugroho, and C. Langhammer, High-performance nanostructured palladium-based hydrogen sensors-current limitations and strategies for their mitigation, *ACS Sens.*, 5(2020), No. 11, p. 3306.

[9] L.R. Xiao, C. Chen, S. Wang, *et al*., Effects of Ti- and Nb-based transition element from single to multiple compound oxides and carbon-based composite additives on Mg–MgH_2 hydrogen storage material, *Tungsten*, 7(2025), No. 1, p. 32.

[10] P. Wu, L.R. Xiao, C.Y. Ge, *et al*., Construction of NiS/carbon fibers confined NiS composite: High catalytic activity for enhancing the hydrogen storage performances of MgH_2, *Rare Met.*, 44(2025), No. 10, p. 7332.

[11] J.O. Abe, A.P.I. Popoola, E. Ajenifuja, and O.M. Popoola, Hydrogen energy, economy and storage: Review and recommendation, *Int. J. Hydrogen Energy*, 44(2019), No. 29, p. 15072.

[12] S. Ghotia, T. Rimza, S. Singh, N. Dwivedi, A.K. Srivastava, and P. Kumar, Hetero-atom doped graphene for marvellous hydrogen storage: Unveiling recent advances and future pathways, *J. Mater. Chem. A*, 12(2024), No. 21, p. 12325.

[13] Y.C. Liu, D. Chabane, and O. Elkedim, Intermetallic compounds synthesized by mechanical alloying for solid-state hydrogen storage: A review, *Energies*, 14(2021), No. 18, art. No. 5758.

[14] B. Zhang, X.B. Xie, Y.K. Wang, *et al*., *In situ* formation of multiple catalysts for enhancing the hydrogen storage of MgH_2 by adding porous $Ni_3ZnC_{0.7}$/Ni loaded carbon nanotubes microspheres, *J. Magnesium Alloys*, 12(2024), No. 3, p. 1227.

[15] S.J. Ding, Y.Q. Qiao, X.C. Cai, *et al*., A novel carbon-induced-porosity mechanism for improved cycling stability of magnesium hydride, *J. Magnesium Alloys*, 13(2025), No. 3, p. 1341.

[16] Y. Zheng, S.L. Yang, B. Hu, *et al*., The enthalpy changes for hydrogenation/dehydrogenation of Mg-based alloys, *J. Magnesium Alloys*, 13(2025), No. 7, p. 2959.

[17] X. Sun, X.H. Yang, Y.F. Lu, *et al*., Hot extrusion-induced Mg–Ni–Y alloy with enhanced hydrogen storage kinetics, *J. Mater. Sci. Technol.*, 202(2024), p. 119.

[18] H.P. Chen, P.N. Hao, J.M. Liu, *et al*., Effect of protective layer from *in situ* heteroatom incorporation on the hydriding reaction of Mg(0001): A density functional theory study, *Int. J. Hydrogen Energy*, 111(2025), p. 113.

[19] M.H. Wu, M.X. Gao, S.Q. Qu, *et al*., $LaVO_4$ prepared by a high-yield method for superior catalysis to the hydrogen storage of MgH_2, *J. Magnesium Alloys*, 13(2025), No. 2, p. 613.

[20] C.G. Lang and X.D. Yao, Enhancing hydrogen storage performance of magnesium-based materials: A review on nanostructuring and catalytic modification, *J. Magnesium Alloys*, 13(2025), No. 2, p. 510.

[21] W.F. Fu, M. Shu, Y.X. Liu, *et al*., Unveiling the micro-mechanism of superior dehydrogenation in γ-MgH_2: Insights into electronic structure of H–Mg bond, *J. Alloy. Compd.*, 1036(2025), art. No. 182130.

[22] X.A. Lu, S.W. Luo, J.Y. Li, *et al*., FIND: A forward–inverse navigation and discovery platform for hydrogen storage alloys powered by data-driven machine learning, *J. Mater. Inf.*, 5(2025), No. 4, p. 48.

[23] H.T. Guan, J. Liu, X. Sun, *et al*., Titanium–nickel dual active sites enabled reversible hydrogen storage of magnesium at 180°C with exceptional cycle stability, *Adv. Mater.*, 37(2025), No. 26, art. No. 2570178.

[24] F.Q. Bu, A. Wajid, N. Yang, *et al*., Fabrication of amorphous TiO_2 hydrogen channels and graphene wrappers to enhance the hydrogen storage properties of MgH_2 with extremely high cycle stability, *J. Mater. Chem. A*, 12(2024), No. 20, p. 12190.

[25] Y. Meng, J. Zhang, S.L. Ju, *et al*., Understanding and unlocking the role of V in boosting the reversible hydrogen storage performance of MgH_2, *J. Mater. Chem. A*, 11(2023), No. 18, p. 9762.

[26] J.H. Cai, Y.T. Jiang, T.A. Yao, *et al*., A demand-driven dynamic heating strategy for ultrafast and energy-efficient MgH_2 dehydrogenation utilizing the "burst effect", *J. Energy Storage*, 130(2025), art. No. 117495.

[27] Z.Y. Dai, P. Wu, L.R. Xiao, *et al*., Non-stoichiometric $Ni_3ZnC_{0.7}$ carbide loading on melamine sponge-derived carbon for hydrogen storage performance improvement of MgH_2, *Rare Met.*, 44(2025), No. 1, p. 515.

[28] W.B. Man, Z.L. Yuan, Z.X. Yang, X.J. Wang, G.X. Fan, and B.Z. Liu, Significantly enhanced kinetics and cyclic stability of MgH_2 by uniquely embedded oxygen vacancy in $Co_2V_2O_7$, *J. Alloy. Compd.*, 1032(2025), art. No. 181137.

[29] Z.Y. Lu, J.H. He, M.C. Song, *et al*., Bullet-like vanadium-based

MOFs as a highly active catalyst for promoting the hydrogen storage property in MgH_2, *Int. J. Miner. Metall. Mater.*, 30(2023), No. 1, p. 44.
[30] Y. Sun, J.Y. Cheng, Y.R. Jiang, Y.F. Liu, and Y.J. Wang, Optimization of Mg-based hydrogen storage materials with multicomponent and high-entropy catalysts, *Int. J. Miner. Metall. Mater.*, 32(2025), No. 11, p. 2699.
[31] S. Bliznakov, E. Lefterova, and N. Dimitrov, Electrochemical PCT isotherm study of hydrogen absorption/desorption in AB_5 type intermetallic compounds, *Int. J. Hydrogen Energy*, 33(2008), No. 20, p. 5789.
[32] B. Cheng, L.J. Kong, H.M. Cai, *et al*., Pushing the Boundaries of solid-state hydrogen storage: A refined study on TiVN-bCrMo high-entropy alloys, *Int. J. Hydrogen Energy*, 60(2024), p. 282.
[33] Q. Li, X. Lin, Q. Luo, *et al*., Kinetics of the hydrogen absorption and desorption processes of hydrogen storage alloys: A review, *Int. J. Miner. Metall. Mater.*, 29(2022), No. 1, p. 32.
[34] M.C. Song, R.K. Xie, L.T. Zhang, *et al*., Combined "Gateway" and "Spillover" effects originated from a $CeNi_5$ alloy catalyst for hydrogen storage of MgH_2, *Int. J. Miner. Metall. Mater.*, 30(2023), No. 5, p. 970.
[35] H.Z. Liu, L. Xu, Y. Han, *et al*., Development of a gaseous and solid-state hybrid system for stationary hydrogen energy storage, *Green Energy Environ.*, 6(2021), No. 4, p. 528.
[36] O.A. Pedroso, W.J. Botta, and G. Zepon, An open-source code to calculate pressure-composition-temperature diagrams of multicomponent alloys for hydrogen storage, *Int. J. Hydrogen Energy*, 47(2022), No. 76, p. 32582.
[37] T.Y. Wang, L. Tang, Y.T. Zhang, *et al*., Interaction between hydrogen and magnesium films: From hydrogenochromism to applications, *ACS Appl. Mater. Interfaces*, 17(2025), No. 6, p. 8794.
[38] M. Victoria, R.J. Westerwaal, B. Dam, and J.L.M. van Mechelen, Amorphous metal-hydrides for optical hydrogen sensing: The effect of adding glassy Ni–Zr to Mg–Ni–H, *ACS Sens.*, 1(2016), No. 3, p. 222.
[39] A. Baldi, D.M. Borsa, H. Schreuders, *et al*., Mg–Ti–H thin films as switchable solar absorbers, *Int. J. Hydrogen Energy*, 33(2008), No. 12, p. 3188.
[40] A. Assila, I. Belkoufa, M. Rkhis, *et al*., Unlocking the hydrogen storage characteristics of MgH_2 hydrides: Investigating the impact of mechanical strain and substitutions, *J. Energy Storage*, 122(2025), art. No. 116708.
[41] C.L. Lu, H.Z. Liu, L. Xu, *et al*., Two-dimensional vanadium carbide for simultaneously tailoring the hydrogen sorption thermodynamics and kinetics of magnesium hydride, *J. Magnesium Alloys*, 10(2022), No. 4, p. 1051.
[42] X.R. Zhao, S.P. Wu, X.M. Chen, *et al*., Mechanism of hydrogenation and dehydrogenation in $Mg/Cu_9Al_4@Mg$ and $MgH_2/Cu_9Al_4@MgH_2$: A DFT and experimental investigation, *J. Alloy. Compd.*, 978(2024), art. No. 173542.
[43] S. Dong, C.Q. Li, E.F. Lv, *et al*., MgH_2/single-atom heterojunctions: Effective hydrogen storage materials with facile dehydrogenation, *J. Mater. Chem. A*, 10(2022), No. 37, p. 19839.
[44] C.Q. Li, W.J. Yang, H. Liu, *et al*., Picturing the gap between the performance and US-DOE's hydrogen storage target: A data-driven model for MgH_2 dehydrogenation, *Angew. Chem. Int. Ed.*, 63(2024), No. 28, art. No. e202320151.
[45] S. Dong, C.Q. Li, J.H. Wang, *et al*., The "burst effect" of hydrogen desorption in MgH_2 dehydrogenation, *J. Mater. Chem. A*, 10(2022), No. 42, p. 22363.
[46] S. Kanagaprabha, A.T. Asvinimeenaatci, R. Rajeswarapalanichamy, and K. Iyakutti, First principles study of pressure induced structural phase transition in hydrogen storage material: MgH_2, *Physica B*, 407(2012), No. 1, p. 54.
[47] M. Bogojeski, L. Vogt-Maranto, M.E. Tuckerman, K.R. Müller, and K. Burke, Quantum chemical accuracy from density functional approximations via machine learning, *Nat. Commun.*, 11(2020), No. 1, art. No. 5223.
[48] G. Kresse and J. Furthmüller, Efficiency of *ab-initio* total energy calculations for metals and semiconductors using a plane-wave basis set, *Comput. Mater. Sci.*, 6(1996), No. 1, p. 15.
[49] G. Kresse and D. Joubert, From ultrasoft pseudopotentials to the projector augmented-wave method, *Phys. Rev. B*, 59(1999), No. 3, p. 1758.
[50] B. Han and F.Y. Li, Regulating the electrocatalytic performance for nitrogen reduction reaction by tuning the N contents in $Fe_3@N_xC_{20-x}$ (x = 0~4): A DFT exploration, *J. Mater. Inform.*, 3(2023), No. 4, art. No. 24.
[51] J.P. Perdew, K. Burke, and M. Ernzerhof, Generalized gradient approximation made simple, *Phys. Rev. Lett.*, 77(1996), No. 18, p. 3865.
[52] A. Vojvodic, J.K. Nørskov, and F. Abild-Pedersen, Electronic structure effects in transition metal surface chemistry, *Top. Catal.*, 57(2014), No. 1-4, p. 25.
[53] V. Wang, N. Xu, J.C. Liu, G. Tang, and W.T. Geng, VASPKIT: A user-friendly interface facilitating high-throughput computing and analysis using VASP code, *Comput. Phys. Commun.*, 267(2021), art. No. 108033.
[54] M. Fox, *Optical Properties of Solids*, Oxford University Press, New York, 2002.
[55] J. Isidorsson, I.A.M.E. Giebels, H. Arwin, and R. Griessen, Optical properties of MgH_2 measured *in situ* by ellipsometry and spectrophotometry, *Phys. Rev. B*, 68(2003), No. 11, art. No. 115112.
[56] K.F. Chen, D.P. Yuan, and Y.Y. Zhao, Review of optical hydrogen sensors based on metal hydrides: Recent developments and challenges, *Opt. Laser Technol.*, 137(2021), art. No. 106808.